

**Original citation:**

Tan, Sze-yin, Perry, David and Unwin, Patrick R.. (2017) Double layer effects in voltammetric measurements with scanning electrochemical microscopy (SECM). Journal of Electroanalytical Chemistry .

**Permanent WRAP URL:**

<http://wrap.warwick.ac.uk/95222>

**Copyright and reuse:**

The Warwick Research Archive Portal (WRAP) makes this work by researchers of the University of Warwick available open access under the following conditions. Copyright © and all moral rights to the version of the paper presented here belong to the individual author(s) and/or other copyright owners. To the extent reasonable and practicable the material made available in WRAP has been checked for eligibility before being made available.

Copies of full items can be used for personal research or study, educational, or not-for-profit purposes without prior permission or charge. Provided that the authors, title and full bibliographic details are credited, a hyperlink and/or URL is given for the original metadata page and the content is not changed in any way.

**Publisher's statement:**

© 2017, Elsevier. Licensed under the Creative Commons Attribution-NonCommercial-NoDerivatives 4.0 International <http://creativecommons.org/licenses/by-nc-nd/4.0/>

**A note on versions:**

The version presented here may differ from the published version or, version of record, if you wish to cite this item you are advised to consult the publisher's version. Please see the 'permanent WRAP url' above for details on accessing the published version and note that access may require a subscription.

For more information, please contact the WRAP Team at: [wrap@warwick.ac.uk](mailto:wrap@warwick.ac.uk)

# Double Layer Effects in Voltammetric Measurements with Scanning Electrochemical Microscopy (SECM)

Sze-yin Tan, David Perry and Patrick R. Unwin\*

*Department of Chemistry, University of Warwick, Coventry CV4 7AL, United Kingdom*

\* To whom correspondence should be addressed. Email: [P.R.Unwin@warwick.ac.uk](mailto:P.R.Unwin@warwick.ac.uk)

Submitted to the special issue in memory of Roger Parsons

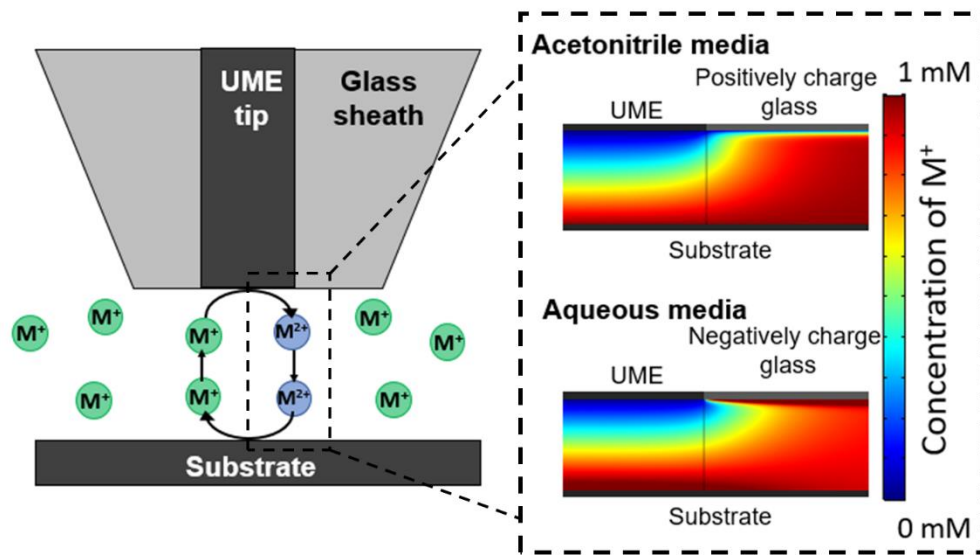
## Abstract

Scanning electrochemical microscopy (SECM) operating as a variable gap ultra-thin layer twin-working electrode cell, has long been recognised as a powerful technique for investigating fast kinetics (heterogeneous electron transfer and homogeneous reactions coupled to electron transfer) as a consequence of high mass transport rates between the working electrodes when biased to promote redox shuttling. Recently, SECM has advanced technically and nanogap cells with dimensions on the 10's nm scale have been reported. In this paper, we consider double layer effects on voltammetric measurements in this configuration, outlining a comprehensive model that solves

the Nernst-Planck equation and Poisson equation with charged interfaces. For supporting electrolyte concentrations that have been used for such measurements (50 mM and 100 mM), it is shown that for typical electrode charges and charge on the glass insulator that encases the ultramicroelectrode (UME) tip used in SECM, there are profound effects on the voltammetric wave-shapes for redox reactions of charged redox couples, in the common modes used to study electron transfer kinetics, namely the tip-voltammetry (feedback mode) and substrate-voltammetry (substrate-generation/tip-collection and competition modes). Using the reduction and oxidation of a singly charged redox species to a neutral and doubly charged species, respectively, as exemplar systems, it is shown that the charge on the electrodes can greatly distort the voltammetric wave-shape, while charge on the glass that surrounds the UME tip can affect the limiting current. This means that the analysis of SECM voltammograms using methods that do not account for double layer effects will result in significant error in the  $k^0$  values derived and tip-substrate distances that have to be estimated from limiting currents in SECM. The model herein provides a framework that could be developed for further studies with nanogap-SECM (e.g. consideration of other models for the electrical double layer, other supporting electrolyte concentrations, potential of zero charge on the electrodes and charges on the redox couples). The model results presented are shown to qualitatively match to SECM voltammetric features from experimental data in the literature, and are further supported by experimental data for redox processes of tetrathiafulvalene (TTF), namely the  $\text{TTF}/\text{TTF}^{\bullet+}$  and  $\text{TTF}^{\bullet+}/\text{TTF}^{2+}$  redox couples. This serves to demonstrate the immediate

practical application of some of the ideas presented herein. For future applications of SECM, the use of different supporting electrolyte concentrations and a range of tip-substrate separations may allow the determination of both electron transfer kinetics and double layer properties.

TOC



## Highlights

- Charged interfaces perturb the local ion concentrations and mass transport in the nanogap-SECM configuration with dual working electrodes.
- Charged interfaces greatly modify the voltammetric response for charged redox couples in SECM.
- Surface charge at both working electrodes, and the glass or quartz encapsulating the SECM tip, needs to be taken into account for a robust analysis of SECM voltammetric data.
- The model framework presented will aid the development of more robust methods to analyse kinetics, double layer effects, mass transport and tip-substrate separations in SECM, especially in a nanogap configuration.

## 1. Introduction

The electrical double layer (EDL) has a pivotal role in electrochemistry and interfacial science and was an area to which Roger Parsons made seminal contributions [1]. Since the initial description of the EDL by Helmholtz [2], many modifications have been proposed including the key early contributions of Gouy-Chapman [3] and Stern [4], resulting in models that have remained popular to this day [1]. In the Gouy-Chapman model, the surface charge is compensated by a diffuse layer of ions in solution and the decay of the electric potential away from the interface is characterised by the Debye length, typically scaling with the inverse square root of the solution ionic strength [5,6]. Note that the Debye length represents the distance over which the electric potential decays to a factor of  $1/e$  of the potential difference between the interface and bulk solution, and does not cover the full dimension of the double layer. Consequently, surface charge effects can be seen at greater distances than the Debye length. The EDL is increasingly recognised to have significant impact on nanoscale electrochemical systems, for which the characteristic diffusion layer size, for a redox reaction involving solutes, approaches that of the EDL [7–20]. The purpose of this paper is to consider the impact of surface charge on scanning electrochemical microscopy (SECM) measurements when configured to create a dual-working electrode thin layer electrochemical cell for kinetic measurements.

SECM has found considerable use in characterising fast heterogeneous electron transfer [21–24], homogeneous (solution) kinetics [25–27], detecting adsorbed species [28–30] and measuring lateral charge transfer [31–35], amongst a wide range of applications. In many of these studies, the gap between the tip and substrate has usually been at the micron or larger scale and, with the excess supporting electrolyte concentrations used, EDL effects are negligible, because the EDL size is very small compared to the gap size (which defines the concentration boundary layer between the two working electrodes). However, recent technical advances have enabled SECM gaps as small as a few 10's of nm to be realised between a parallel dual-working electrode arrangement (so-called “nanogap-SECM”) [36,37], which provides ultrafast diffusion rates of redox species between the two working electrodes as seen in other nanogap devices [15,38,39]. In principle, this is highly advantageous for the study of fast kinetics, but the high surface area to solution volume ratio of such devices magnifies certain physicochemical effects, including adsorption [30,40] and, as we show herein, EDL phenomena. EDL effects have been explored very recently for dual-electrode nanogap devices [15,16], and for SECM [17] but in the latter case with the focus on the active part of the tip and substrate electrodes and for the highly charged  $\text{Fe}(\text{CN})_6^{4-}$  couple. These studies highlight that the voltammetric wave-shape recorded at the dual-electrodes can be significantly modified by EDL properties, with the effect being most noticeable (as expected) at low electrolyte concentration and/or small gap size where the EDL size is non-negligible. However, EDL effects are still seen at ionic strengths that are more typically used in



voltammetry (e.g. 0.1 to 1.0 M 1:1 electrolyte concentration in both aqueous solution [16,17] and acetonitrile [15]).

The UME tip electrode in SECM is encased in an insulating sheath that is often fabricated from glass or quartz and has traditionally been considered to be ‘inert’ [41]. However, in a recent paper [30], we have demonstrated that the glass sheath can influence transient mass transport during SECM measurements [30]. Given the strong ion current rectification (ICR) effects that are seen in glass and quartz nanopipettes [42–45] of characteristic dimensions similar to, and larger, than the gap size in nanogap-SECM, and that surface induced ion current rectification (SIR) phenomena are seen in scanning ion conductance microscopy (SICM) studies of charged interfaces [46–50], at ionic strengths similar to those used in typical SECM voltammetric measurements, it is essential to investigate surface charge and EDL effects from the glass sheath of the SECM tip, as well as from the electrodes. Primarily through modelling, but also with some experiments, we demonstrate that EDL effects in nanogap-SECM are very significant and need to be accounted for when analysing SECM data from a variety of different modes, e.g. the tip-voltammetry [21,22] and substrate-voltammetry [23,30] modes. We also point out instances in the literature where features arising from the models outlined herein are clearly evident in experimental voltammetric data, but have either been ignored or interpreted in terms of other phenomena.

## 2. Theory and Simulations

COMSOL Multiphysics 5.2a (COMSOL, Stockholm, Sweden) finite-element method modelling software was used to describe the time-dependent mass transport problem in a 2D-axisymmetric cylindrical SECM configuration shown in Figure 1.

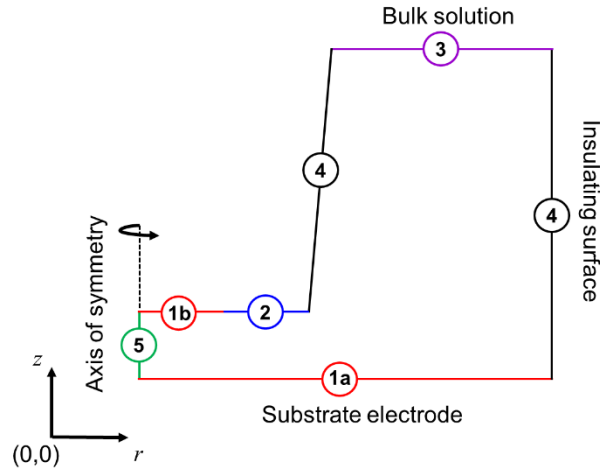


Figure 1. Schematic of the 2D-axisymmetric SECM simulation domain (not to scale), with labelled boundaries 1a and 1b (red) being the substrate and tip electrode surfaces, respectively, label 2 (blue) represents the glass surface that encapsulates the UME tip, label 3 (purple) is the bulk solution, label 4 (black) is a no-flux boundary and label 5 (green) is the axis of symmetry.

For this purpose, the Nernst-Planck equation was solved to describe the mass transport of all species in solution:

$$\frac{\partial c_i}{\partial t} = \nabla \cdot \left( D_i \nabla c_i + z_i \frac{F}{RT} D_i c_i \nabla \phi \right) \quad (1)$$

and the Poisson equation described the electrical potential,  $\phi$ :

$$\nabla^2 \phi = \frac{F}{\varepsilon \varepsilon_0} \sum z_i c_i \quad (2)$$

where  $c_i$ ,  $D_i$  and  $z_i$  denote the concentration, diffusion coefficient and charge of species  $i$  in solution, respectively.  $\varepsilon$  is the solvent dielectric constant (38 for acetonitrile, 78 for water) and  $\varepsilon_0$  is the vacuum permittivity ( $8.85 \times 10^{-12}$  F m<sup>-1</sup>).  $F$ ,  $R$  and  $T$  are the Faraday constant (96485 C mol<sup>-1</sup>), gas constant (8.31 J mol<sup>-1</sup> K<sup>-1</sup>) and absolute temperature (298 K), respectively.

We first consider TTF, which undergoes two sequential single electron oxidation processes in acetonitrile media [51], as an exemplar, for which we also report experimental data (*vide infra*):



where  $k_{\text{ox}}$  and  $k_{\text{red}}$  are the first-order heterogeneous oxidation and reduction rate constants, respectively. Subscripts 1 and 2 refer to the TTF/TTF<sup>•+</sup> and TTF<sup>•+</sup>/TTF<sup>2+</sup> redox processes, respectively.

Both the TTF/TTF<sup>•+</sup> and TTF<sup>•+</sup>/TTF<sup>2+</sup> redox processes are studied in the tip-voltammetry mode of SECM. This follows from a previously reported total shielding approach [25,52] where a large substrate electrode was held at a potential,  $E_{\text{sub}}$ , ( $E_{\text{TTF}/\text{TTF}^{\bullet+}}^{0'} < E_{\text{sub}} < E_{\text{TTF}^{\bullet+}/\text{TTF}^{2+}}^{0'}$ ). This creates a quasi-steady-state diffusion layer of TTF<sup>•+</sup> extending from the substrate electrode surface and shields the UME tip, which is placed close to the substrate surface, from the bulk TTF solution. TTF<sup>•+</sup> reduction to TTF, on the one hand, and oxidation to TTF<sup>2+</sup>, on the other, at the UME tip

can thus be investigated from the gap solution essentially free from the influence of the comproportionation reaction, between TTF (from bulk solution) and  $\text{TTF}^{2+}$  (tip-generated) species [25,52]. In this way,  $\text{TTF}^{\bullet+}$  reduction and oxidation reactions, under the same (mass transport) conditions [53], would be expected to yield equal but opposite limiting currents if diffusional mass transport alone were operating. The electrolyte solution (acetonitrile) also contains a supporting electrolyte comprising of 0.1 M tetrabutylammonium hexafluorophosphate ( $\text{TBAPF}_6$ ).

The first-order heterogeneous oxidation and reduction rate constants are described by the Butler-Volmer relationship, but with the plane of electron transfer (PET) taken to be the Outer Helmholtz Plane, located 0.6 nm from the actual electrode surface, as considered in recent work from other groups [15–17]. The flux at the substrate PET (Figure 1, Label 1a) is described by:

$$J_{\text{TTF}} = -k_1^0 c_{\text{TTF}} e^{\left[(1-\alpha_1)\frac{F}{RT}(E_{\text{sub}}-\phi-E_1^{0'})\right]} + k_1^0 c_{\text{TTF}^{\bullet+}} e^{\left[(-\alpha_1)\frac{F}{RT}(E_{\text{sub}}-\phi-E_1^{0'})\right]} \quad (4a)$$

$$J_{\text{TTF}^{2+}} = k_2^0 c_{\text{TTF}^{\bullet+}} e^{\left[(1-\alpha_2)\frac{F}{RT}(E_{\text{sub}}-\phi-E_2^{0'})\right]} - k_2^0 c_{\text{TTF}^{2+}} e^{\left[(-\alpha_2)\frac{F}{RT}(E_{\text{sub}}-\phi-E_2^{0'})\right]} \quad (4b)$$

$$J_{\text{TTF}^{\bullet+}} = -J_{\text{TTF}} - J_{\text{TTF}^{2+}} \quad (4c)$$

$$J_{\text{TBA}^+} = J_{\text{PF}_6^-} = 0 \quad (4d)$$

where  $k_i^0$ ,  $\alpha_i$  and  $E_i^{0'}$  refer to the standard electron transfer rate constant, transfer coefficient and formal potential, respectively,  $E_{\text{sub}} - \phi$  refers to the potential drop across the Helmholtz layer at the substrate electrode. Similarly, the flux to the UME tip PET (Figure 1, Label 1b) is given by:

$$J_{\text{TTF}} = -k_1^0 c_{\text{TTF}} e^{\left[(1-\alpha_1)\frac{F}{RT}(E_{\text{UME}} - \phi - E_1^{0'})\right]} + k_1^0 c_{\text{TTF}^{\bullet+}} e^{\left[(-\alpha_1)\frac{F}{RT}(E_{\text{UME}} - \phi - E_1^{0'})\right]} \quad (5a)$$

$$J_{\text{TTF}^{2+}} = k_2^0 c_{\text{TTF}^{\bullet+}} e^{\left[(1-\alpha_2)\frac{F}{RT}(E_{\text{UME}} - \phi - E_2^{0'})\right]} - k_2^0 c_{\text{TTF}^{2+}} e^{\left[(-\alpha_2)\frac{F}{RT}(E_{\text{UME}} - \phi - E_2^{0'})\right]} \quad (5b)$$

$$J_{\text{TTF}^{\bullet+}} = -J_{\text{TTF}} - J_{\text{TTF}^{2+}} \quad (5c)$$

$$J_{\text{TBA}^+} = J_{\text{PF}_6^-} = 0 \quad (5d)$$

where  $E_{\text{UME}}(t)$  refers to the time-dependent potential applied to the UME tip given by:

$$0 \leq t \leq t_s: E_{\text{UME}}(t) = E_{\text{init}} + \nu t \quad (6a)$$

$$t_s < t \leq 2t_s: E_{\text{UME}}(t) = E_{\text{init}} + 2\nu t_s - \nu t \quad (6b)$$

where  $E_{\text{init}}$  is the initial potential applied to the electrode,  $\nu$  is the potential scan rate and  $t_s$  is the time taken to complete a potential sweep in one direction. Note that for this problem, for illustrative purposes, we considered the standard rate constant for a particular couple to be the same at the two electrodes, but setting different rate constants would be trivial.

The potential drop across the Helmholtz layer at both the substrate electrode (Figure 1, Label 1a) and UME tip (Figure 1, Label 1b) surface results in surface charge density,  $\rho$ , given by [15,16]:

$$\rho_{\text{sub}} = (E_{\text{sub}} - \phi) \frac{\varepsilon_{\text{HL}} \varepsilon_0}{d_{\text{HL}}} \quad (7)$$

and

$$\rho_{\text{UME}} = (E_{\text{UME}} - \phi) \frac{\varepsilon_{\text{HL}} \varepsilon_0}{d_{\text{HL}}} \quad (8)$$

where  $\varepsilon_{\text{HL}} = 6$  is a reasonable dielectric constant of the Helmholtz layer [15] in acetonitrile. We briefly consider the effect of a larger value of  $\varepsilon_{\text{HL}} = 10$  below.

The charge on the glass surface encasing the UME tip electrode (Figure 1, Label 2) is also considered in this work and is given by  $\rho = \rho_{\text{G}}$ , where  $\rho_{\text{G}}$  is the surface charge density of borosilicate glass in acetonitrile measured experimentally (*vide infra*).

Other initial and boundary conditions shown in Figure 1 are as follows:

Label 3 (Bulk solution)  $c_{\text{TTF}} = 1.0 \text{ mM}$ ,  $c_{\text{TTF}^{•+}} = c_{\text{TTF}^{2+}} = 0.0 \text{ mM}$ ,  $c_{\text{P}} = c_{\text{N}} = 0.1 \text{ M}$ ,  $\phi = 0.0 \text{ V}$ . As pointed out in other work [15], there is some variability in values reported for the PZC of platinum electrodes, and a sparsity of data for acetonitrile solution. However, careful studies of the effect of PZC on voltammetry in a nanogap cell have shown that the resulting features in simulated voltammograms are qualitatively similar for a range of different PZC values [15]. It is reasonable

to assume that the Ag quasi-reference electrode (QRE) used experimentally herein is similar to the Ag/AgCl reference scale [54], especially as we are dealing with relatively large potentials relative to the PZC. Consequently, the potential of zero charge (PZC) of the electrodes was set to be 0.0 V for all simulations considered herein, as for other work in acetonitrile solution [15].

Label 4 (Insulating boundaries):  $J_{\text{TTF}} = J_{\text{TTF}^{\bullet+}} = J_{\text{TTF}^{2+}} = J_{\text{TBA}^+} = J_{\text{PF}_6^-} = 0, \rho = 0$ .

Label 5: Axis of symmetry

The current is calculated from the following:

$$i = 2\pi F \int (2J_{\text{TTF}} + J_{\text{TTF}^{\bullet+}}) r dr \quad (9)$$

A list of parameters used is given in Table S-1 (SI, Section S-1).

Through the use of simulations only, we also consider the implications of the electrode and glass surface charge on the paired voltammetric response of substrate-voltammetry SECM in typical nanogap geometries in aqueous solution. Simulation details for this part of the work are similar to those above, except that the standard rate constant of the redox couple at the tip and substrate was allowed to be different. The model is reported in the SI, Section S-2, with the results reported herein.

### 3. Experimental Methods

#### 3.1 Chemicals

TTF and TBAPF<sub>6</sub> were purchased from Sigma-Aldrich and used without further purification. Acetonitrile (Fisher, HPLC grade) was dried using 3 Å molecular sieves prior to use. The concentration of TTF solutions for all experiments was 1.0 mM in acetonitrile with 0.1 M TBAPF<sub>6</sub> as the supporting electrolyte.

#### 3.2 Electrode Materials

A Pt disk macroelectrode of 2.0 mm-diameter was obtained from CH Instruments, Inc and served as the substrate working electrode. The tip working electrode was a Pt disk UME that was fabricated in-house using an established procedure [55], involving heat sealing a 2.0 µm-diameter Wollaston Wire (Goodfellow, Huntington, UK), with the Ag layer removed from the end section [55], in a borosilicate glass capillary under vacuum. The end of the UME was polished conically and flat to obtain an RG value (ratio of radius of the encapsulating glass- from the electrode centre- to that of the active disk electrode) of ca. 10. Before use, both electrodes were polished with alumina (50 nm) on a soft microfibre polishing pad (MicroCloth, Buehler Ltd.) followed by a clean wet microfiber pad, and then dried to produce the finished electrode surface. Ag and Pt wires served as the QRE and counter electrode, respectively. The potential of the Ag QRE was stable on the timescale of the voltammetric measurements.



### 3.3 Nanopipettes and nanopipette voltammetry

Borosilicate glass single barrel capillaries (o.d. 1.2 mm, i.d. 0.69 mm, Harvard Apparatus) were pulled using a laser puller (P-2000, Sutter Instruments) with the following pulling parameters: (line 1) – Heat 330, Fil 3, Vel 30, Del 220 and Pul 0; (line 2) – Heat 330, Fil 3, Vel 40, Del 220, Pul 120. Dimensions of the individual nanopipettes used in the experiments were measured using scanning electron microscopy and were ca. 200 nm in diameter at the end. The instrumentation used for nanopipette voltammetry has been previously reported [44,47–49]. The current was measured using a custom current-to-voltage converter, while data recording and potential output control was performed using a custom written LabVIEW (2013, National Instruments) program through an FPGA card.

The nanopipettes were filled and bathed in acetonitrile containing 1.0 mM TBAPF<sub>6</sub> electrolyte, the low concentration accentuating charge effects and hence giving the most accurate estimation for the glass surface charge. An Ag quasi-reference-counter electrode (QRCE) was inserted into the back of the nanopipette and a second similar QRCE was placed in the bulk solution. The potential applied to the QRCE inserted into the nanopipette was swept from -0.5 V to 0.5 V with respect to the QRCE in bulk at a scan rate of 50 mV s<sup>-1</sup> and the current was recorded at the QRCE in the bulk solution.

### 3.4 SECM Instrumentation

An intermittent-contact SECM setup was used for tip-voltammetry SECM measurements as previously reported [56]. Briefly, a home-built SECM was mounted onto a vibration-isolation table inside a Faraday cage. The UME was attached to a piezo bender actuator to which an oscillation of 70 Hz with an amplitude of 50 nm ( $\sim 5\%$  of the UME active electrode size) was applied. This was, in turn, mounted onto a 3D-piezoelectric positioner controlled by a PC running custom LabVIEW code (LabVIEW 9.0, National Instruments), which was also used for data acquisition. To set the tip-substrate distance, the tip was approached to the substrate electrode ( $0.05\ \mu\text{m s}^{-1}$ ) and tip-substrate intermittent-contact was detected by the damping ( $\sim 5\%$ ) of the tip oscillation amplitude, at which point the tip ceased to move. The  $z$ -position oscillation was switched off and the tip was retracted by a defined distance of interest to set the gap size, which was determined precisely via limiting current measurements using a procedure described herein.

## 4. Results and Discussion

### 4.1 Nanopipette voltammetry in acetonitrile media

Nanopipette voltammetry was used to quantify the surface charge density of borosilicate glass pipette walls by determining the ICR effect, whereby a bias applied between the QRCE in the nanopipette and a second QRCE located in the bulk solution, scanned linearly with time, produces a non-ohmic current response. The extent of rectification is highly sensitive to the surface charge

present on the internal walls of the nanopipette and the nanopipette dimensions [44,57]. ICR arises due to a combination of a permselective region that is formed at the end of the nanopipette, as a result of the wall charge, coupled with an asymmetry of mass transport of ions inside (predominantly linear migration) and outside (spherical transport) of the nanopipette domain [42,44,45,47,50,57,58]. When the EDL is non-negligible compared to the tip opening size, the charged nanopipette exhibits selectivity toward the counterions of the EDL. Thus, for example, for a positively charged nanopipette, when a positive bias is applied to the nanopipette electrode, with respect to bulk, anions will accumulate inside the tip of the nanopipette (with cation charge balance). This results in a higher conductance state inside the nanopipette and an enhanced ionic current is seen. Alternatively, with a negative bias applied, a depletion zone forms at the nanopipette end as anions tend to move away from the pipette opening faster than transport inside the pipette, resulting in a lower conductance state [45,47,49,50,57,58]. For a negatively charged nanopipette (as typical in nanopipette and SICM aqueous conditions) [58], this phenomenon occurs with the opposite electrode polarity, with the nanopipette end having selectivity for cations.

Figure 2 shows the experimental current-voltage (black line) characteristic for a 200 nm-diameter borosilicate glass nanopipette in an acetonitrile solution containing 1.0 mM TBAPF<sub>6</sub> electrolyte. Following the arguments outlined above, the enhancement of ionic current at positive tip potentials compared to negative tip potentials is indicative of positively charged nanopipette walls.

FEM simulations were used to analyse and quantify the nanopipette voltammogram using a previously reported model [44] for nanopipette surface charge characterisation (see SI, Section S-3 for details). Geometrical parameters obtained from TEM images of the nanopipette were used. The experimental curve shows good agreement with a simulated surface charge density of  $+10 \text{ mC m}^{-2}$  (Figure 2). This result is consistent with previously reported ICR studies at quartz nanopipettes in various organic media which also described the effect of tip size, electrolyte concentration and water content on the response [59].

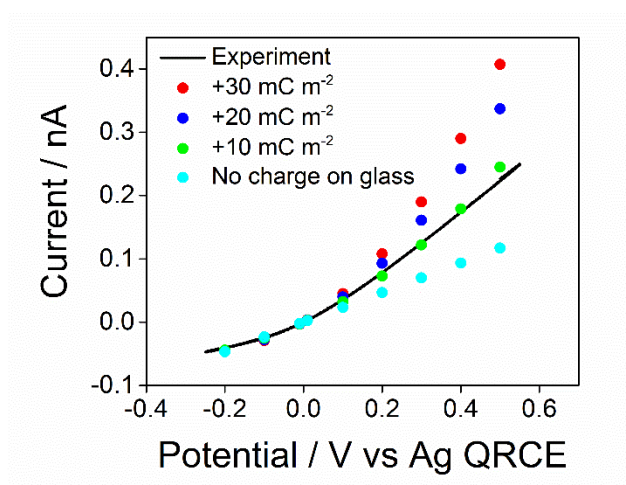


Figure 2. Current-potential characteristic for a 200 nm-diameter borosilicate nanopipette at low ionic strength (1.0 mM TBAPF<sub>6</sub>) in acetonitrile solution showing ion current rectification. The simulated current-potential responses for a range of surface charge densities applied to the nanopipette walls are also shown (see inset key). The simulation with a surface charge density of  $+10 \text{ mC m}^{-2}$  shows a good match to the experimental response.

At higher electrolyte concentrations (e.g. 100 mM), the size of the EDL is negligible compared to the nanopipette opening size, resulting in minimal ICR effects as shown in Supporting

Information (SI), Figure S-3. For the SECM experimental conditions considered here (100 mM supporting electrolyte concentration and ca. 300 nm tip-substrate separation), EDL effects at the glass sheath of the tip are thus unlikely to perturb the local concentration in the nanogap and to distort the voltammetric response (further considered in SI, Section S-4). However, the measured surface charge density of  $+10 \text{ mC m}^{-2}$  on borosilicate glass in acetonitrile solutions was included in the development of a holistic SECM model for surface charge effects (*vide supra*) and in the results in the following section (Section 4.2). Surface charge on the UME glass is further considered in Section 4.3 for a typical nanogap-SECM configuration, where it is shown to be important.

#### 4.2 Tip-voltammetry (total-shielding) SECM experiments and simulations

Tip-voltammetry SECM was employed for  $\text{TTF}^{\bullet+}$  reduction to TTF and  $\text{TTF}^{\bullet+}$  oxidation to  $\text{TTF}^{2+}$  in acetonitrile containing 1 mM TTF in bulk and 0.1 M TBAPF<sub>6</sub> as supporting electrolyte. A typical set of voltammograms at 3 different tip-substrate separations is shown in Figure 3. The distances were determined from the positive feedback limiting current (SI, Section S-4) [60], and the tip currents were normalised with respect to the steady-state diffusion-limited tip current for the oxidation of TTF to  $\text{TTF}^{\bullet+}$  in the bulk solution. The large substrate electrode was held at a fixed potential,  $E_{\text{sub}}$ , of 0.55 V vs Ag QRE to generate a quasi-steady-state diffusion layer of  $\text{TTF}^{\bullet+}$  at the substrate electrode surface from the bulk TTF solution. The UME tip (radius,  $a = 1.0 \text{ }\mu\text{m}$ ) was positioned at a known fixed distance from the Pt substrate surface and its potential,  $E_{\text{UME}}$ , was

swept from 0.1 V to 1.0 V at a sweep rate of 50 mV s<sup>-1</sup>. At  $E_{\text{UME}} \ll 0.55$  V, the tip reduced  $\text{TTF}^{\bullet+}$  to TTF, giving a cathodic current response while at  $E_{\text{UME}} \gg 0.55$  V, the tip oxidised  $\text{TTF}^{\bullet+}$  to  $\text{TTF}^{2+}$ , giving an anodic current response. As the UME tip was close to the substrate surface, it was essentially completely shielded from the bulk TTF solution. Hence, the homogeneous comproportionation reaction between tip-generated  $\text{TTF}^{2+}$  and bulk TTF does not occur to any significant extent in this configuration [25,52].

The voltammograms for both the reduction of  $\text{TTF}^{\bullet+}$  to TTF and the oxidation of  $\text{TTF}^{\bullet+}$  to  $\text{TTF}^{2+}$  show increasing limiting current at decreasing tip-substrate separations due to enhanced redox cycling (akin to positive feedback) [61]. Under steady-state diffusional mass transport limits, the reductive and oxidative limiting currents ( $i_{\text{lim,red}}$  and  $i_{\text{lim,ox}}$ , respectively) are predicted to be equal but opposite, controlled by the diffusional flux of  $\text{TTF}^{\bullet+}$  ( $J = D_{\text{TTF}^{\bullet+}} \nabla c_{\text{TTF}^{\bullet+}}$ ) [53]. However, this is clearly not the case experimentally. Instead, considerable asymmetry of the oxidative and reductive limiting currents is seen. Notably, the current for the reduction of  $\text{TTF}^{\bullet+}$  is always considerably larger than for the oxidation of  $\text{TTF}^{\bullet+}$  at all tip-substrate distances measured, with the ratio of  $i_{\text{lim,red}}/i_{\text{lim,ox}}$  increasing with decreasing tip-substrate separation. This is attributed to the EDL effect from the tip and substrate electrodes, as discussed further below.

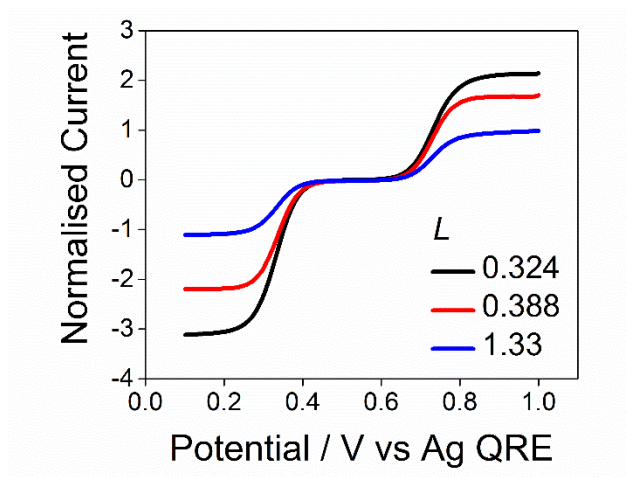


Figure 3. Experimental UME tip linear sweep voltammograms recorded in an SECM configuration for the reduction and oxidation of  $\text{TTF}^{\bullet+}$  generated at a large Pt substrate electrode (held at a fixed potential of 0.55 V vs Ag QRE with a 20 s electrogeneration time before the commencement of the tip LSV) from 1.0 mM TTF in acetonitrile (0.1 M TBAPF<sub>6</sub>) bulk solution. A 1.0  $\mu\text{m}$ -radius Pt UME tip (RG = 10) was positioned above the 1.0 mm-radius Pt disk substrate (aligned approximately over the centre) at normalised tip-substrate distances,  $L = 0.324$  (black), 0.387 (red) and 1.33 (blue). These correspond to gap sizes of 324 nm, 387 nm and 1.33  $\mu\text{m}$ , respectively. The tip potential was scanned between 0.1 V and 1.0 V vs Ag QRE at a scan speed of 50 mV s<sup>-1</sup>.

The significance of EDL effects on the tip voltammetric response was explored herein by solution of the Nernst-Planck and Poisson equations in COMSOL Multiphysics (*vide supra*). Throughout, we have chosen a Gouy-Chapman model for the EDL at glass surfaces (diffuse double layer (DDL) model), as has been used in many ICR studies with concentrations up to 0.1 M [42,45,57]. In general, the Gouy-Chapman model can only reasonably be applied for low ionic strengths and where small surface potentials are involved. Where the surface charge that manifests is due to a fixed number of sites, as would be the case for insulating glass nanopipettes, the ion concentrations near the surface will be limited, even at moderate to high ionic strengths and

consequently the Gouy-Chapman model has been considered to be reasonable at 1:1 electrolyte concentrations of up to 0.1 M and moderate surface charge densities [3,5,28,62]. Validation of the Gouy-Chapman model can be found in surface force measurements that have demonstrated that the potential profile fits the Gouy-Chapman model at separations of greater than 2 nm from the surface in electrolyte concentrations of up to 0.1 M (and closer distances were not probed) [5]. Where surface charge is considered on electrode surfaces, as discussed in the next section, a modification to this model was included, whereby a thin region of 0.6 nm from the electrode (Helmholtz layer) was assigned a small value of  $\epsilon_{\text{HL}}$  yielding an intensification of the electric field. The potential at the outer Helmholtz plane was calculated and subtracted from the applied potential to represent the drop across the Helmholtz layer (see eq 7 and 8 in Section 2), effectively resulting in a Gouy-Chapman-Stern model for the EDL [16,17]. This was considered reasonable for the electrode surfaces, as the surface charge densities (at large applied potential) can be much higher than that at the glass (e.g.  $\sim 100 \text{ mC/m}^2$  at 1 V). As we pointed out earlier in the paper, this model and approach yields semi-quantitative information of double layer effects in SECM, which is the intention.

As discussed in Section 2, the EDL parameters used are approximate and were taken from related work (*vide supra*) [15,17]. Figure 4 shows the simulated tip current-potential response for a UME tip which has a radius,  $a = 1.0 \text{ }\mu\text{m}$ , with  $\text{RG} = 10$  held at a typical normalised tip-substrate separations of  $L = 0.3, 0.4$  and  $1.3$ . The following parameters apply:  $k_1^0 = k_2^0 = 30 \text{ cm s}^{-1}$  (Figure



4a) and  $k^0_1 = k^0_2 = 100 \text{ cm s}^{-1}$  (Figure 4b) (the same  $k^0$  values were used for both UME and substrate surfaces for illustrative purposes, as highlighted earlier),  $\alpha_1 = \alpha_2 = 0.5$ ,  $D_{\text{TTF}} = 2.1 \times 10^{-5} \text{ cm}^2 \text{ s}^{-1}$ ,  $D_{\text{TTF}^{\bullet+}} = 1.90 \times 10^{-5} \text{ cm}^2 \text{ s}^{-1}$ ,  $D_{\text{TTF}^{2+}} = 1.60 \times 10^{-5} \text{ cm}^2 \text{ s}^{-1}$ ,  $D_{\text{TBA}^+} = 1.5 \times 10^{-5} \text{ cm}^2 \text{ s}^{-1}$ ,  $D_{\text{PF}_6^-} = 1.7 \times 10^{-5} \text{ cm}^2 \text{ s}^{-1}$ ,  $c_{\text{TTF}} = 1.0 \text{ mM}$ ,  $c_{\text{TBA}^+} = c_{\text{PF}_6^-} = 0.1 \text{ M}$ ,  $z_{\text{TTF}} = 0$ ,  $z_{\text{TTF}^{\bullet+}} = +1$ ,  $z_{\text{TTF}^{2+}} = +2$ ,  $z_{\text{TBA}^+} = +1$ ,  $z_{\text{PF}_6^-} = -1$  and  $\nu = 50 \text{ mV s}^{-1}$ .

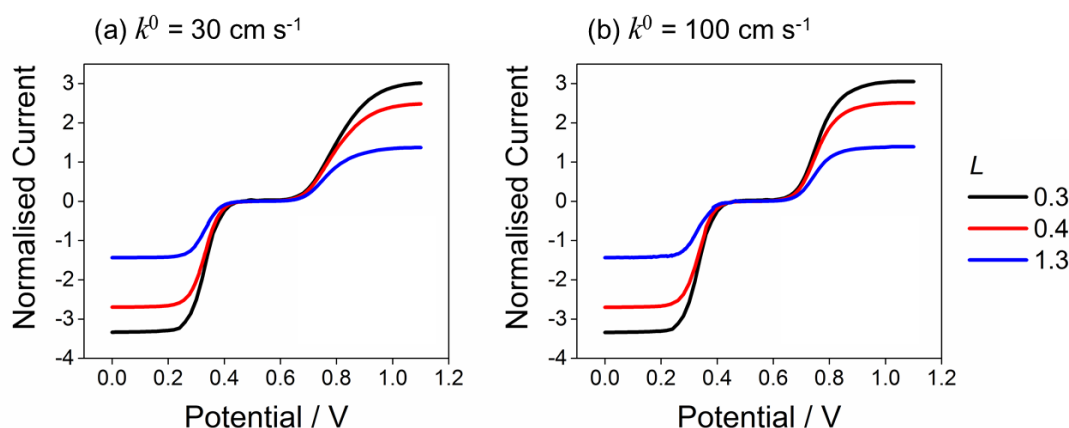


Figure 4. Simulated tip current response for the reduction and oxidation of 1.0 mM  $\text{TTF}^{\bullet+}$  with (a)  $k^0_1 = k^0_2 = 30 \text{ cm s}^{-1}$  and (b)  $k^0_1 = k^0_2 = 100 \text{ cm s}^{-1}$ .  $\text{TTF}^{\bullet+}$  was generated at a large Pt substrate electrode (held at a fixed potential of 0.55 V vs Ag QRE) from 1.0 mM TTF in acetonitrile (100 mM TBAPF<sub>6</sub>) at different tip-substrate separations ( $L = 0.3, 0.4$  and  $1.3$ ). The simulated currents in the SECM configuration are normalised to the simulated diffusion limiting current for the oxidation of TTF to  $\text{TTF}^{\bullet+}$  at the UME tip in bulk solution. Other simulation parameters are summarised in the text.

For all tip-substrate distances considered, the simulated voltammograms reproduce the experimentally observed trend of larger reductive wave magnitude compared to the oxidative wave limiting current, with the difference between the anodic and cathodic magnitudes exacerbated at closer tip-substrate separations.

It is also important to point out that Figure 4a shows an oxidative wave with apparently slow kinetics compared to the reduction wave, even though they have the same simulated kinetic parameters ( $k_1^0 = k_2^0 = 30 \text{ cm s}^{-1}$  and  $\alpha_1 = \alpha_2 = 0.5$ ). The oxidation wave is drawn out on the potential scale, with the half wave potential shifted towards higher overpotential, an effect which is also seen experimentally in Figure 3, where the difference between the quarter-wave and three quarter-wave potentials of the current sigmoidal (inter-quartile potential) of the reduction and oxidation wave are found to be 60 and 68 mV, respectively, at  $L = 0.324$ , rather than 59 mV expected for a reversible process [63]. This is mainly due to introducing the PET at the OHP (Frumkin double layer correction). Simulations were also performed with a dielectric constant of 10 applied in the Frumkin correction, as there is evidence in the literature that the permittivity of the Helmholtz layer may be larger in acetonitrile [64]. The obtained voltammograms from these simulations are presented in Supporting Information, Figure S-5 and show a much more drawn out oxidative wave. It is worth noting that although the effect of this change in permittivity does not produce a similar voltammogram to that obtained experimentally, by adjusting other parameters, it may be possible to obtain a reasonable fit. This was not attempted herein.

Interestingly, the effects that we have highlighted in this section have been seen in studies of the oxidation and reduction of tris(2,2'-bipyridine)ruthenium (II) (Ru(byp)) in acetonitrile, studied by the SECM feedback mode with gap sizes (0.45 – 2.0  $\mu\text{m}$ ) similar to those considered herein and with the same supporting electrolyte (0.1 M TBAPF<sub>6</sub>) [24]. Significant differences

were seen between the apparent kinetics deduced from oxidation and reduction waves using conventional ET models. This different behaviour was interpreted as being due to different oxidation and reduction mechanisms. Yet, the experimental observations were, in fact, similar to those found herein: (i) for smaller gap sizes of 0.45 – 0.75  $\mu\text{m}$ , the oxidation voltammograms were somewhat complicated, with sloped limiting currents, rather than conventional plateaus, and rather extreme transfer coefficients were needed in order to fit the experimental data to conventional models. (ii) In contrast, for larger gap sizes, the Ru(byp) oxidation response tended to Nernstian behaviour. (iii) The reduction limiting current magnitude was found to be about 20 % larger than to the oxidation current even though the two voltammograms were measured at the same tip-substrate distance. In this case, the oxidation potential was such that the tip electrode would be highly positively charged whereas for the reduction it would have been highly negatively charged, and this behaviour, and apparent difference in electron transfer kinetics, is consistent with the double layer effects highlighted herein.

#### 4.3 Simulated surface charge effects on nanogap-SECM voltammetric responses

We now consider the commonly used substrate-voltammetry SECM configuration for a generic single electron oxidation process in aqueous solution (also containing the cation,  $\text{Cat}^+$ , and the anion,  $\text{An}^-$ , of the supporting electrolyte) given by the following:



as a relevant example. This might be represented by the  $\text{TTF}^{\bullet+/2+}$  couple discussed above or the ferrocenylmethyl trimethylammonium couple ( $\text{FcTMA}^{+/2+}$ ) couple which is commonly used to study a wide range of electrode materials as a fast outer-sphere redox couple [30,36,54,65]. The potentials reported in this section are representative of a typical aqueous reference electrode scale such as Ag/AgCl.

In this configuration, an SECM tip is positioned close to a larger substrate electrode surface to amperometrically detect the reactants or products of the substrate electrode reaction under high mass transport conditions. This results in a pair of substrate-generation/tip-collection (SG/TC) and competition mode tip-current vs substrate-potential curves [23,30,66] which – in principle – can be used to determine fast ET rate constants as well as the tip-substrate separation and diffusion coefficient ratios [23,24,67,68]. A schematic of the substrate-voltammetry SECM operation protocol is shown in SI, Section S-2, Figure S-1.

Parameters typical of the nanogap-SECM geometry were considered, with a UME tip of radius,  $a = 0.5 \mu\text{m}$  with  $\text{RG} = 2$ , held at normalised tip-substrate separations,  $L = 0.1 - 0.3$  [30,36]. The following parameters apply throughout:  $k_{\text{UME}}^0 = 100 \text{ cm s}^{-1}$  (fixed and corresponding to ultrafast kinetics),  $k_{\text{sub}}^0$  was varied (*vide infra*),  $\alpha = 0.5$ ,  $D_{\text{M}^+} = D_{\text{M}^{2+}} = 1.0 \times 10^{-5} \text{ cm s}^{-1}$ ,  $D_{\text{Cat}^+} = D_{\text{An}^-} = 2.0 \times 10^{-5} \text{ cm s}^{-1}$ ,  $c_{\text{M}^+} = 1.0 \text{ mM}$ ,  $c_{\text{Cat}^+} = c_{\text{An}^-} = 5 \text{ mM}$ ,  $z_{\text{M}^+} = +1$ ,  $z_{\text{M}^{2+}} = +2$ ,  $z_{\text{Cat}^+} = +1$ ,  $z_{\text{An}^-} =$

-1,  $E^{0'} = 0.4 \text{ V}$  and  $\nu = 0.05 \text{ V s}^{-1}$ . These parameters are similar to those used in previous experimental studies [30]. Simulation details can be found in SI, Section S-2.

#### 4.3.1. Effect of charge on glass on paired nanogap voltammograms

Figure 5 shows simulated tip-current vs substrate-potential curves for the competition and SG/TC modes for a range of surface charge densities (+30 to -30  $\text{mC m}^{-2}$ ) at the glass surface that encapsulates the UME tip for the case where there is no charge on the electrode surface to highlight any effect of the glass charge (Figure 5a) and then where surface charge effects are considered on both the UME and substrate electrodes (Figure 5b).

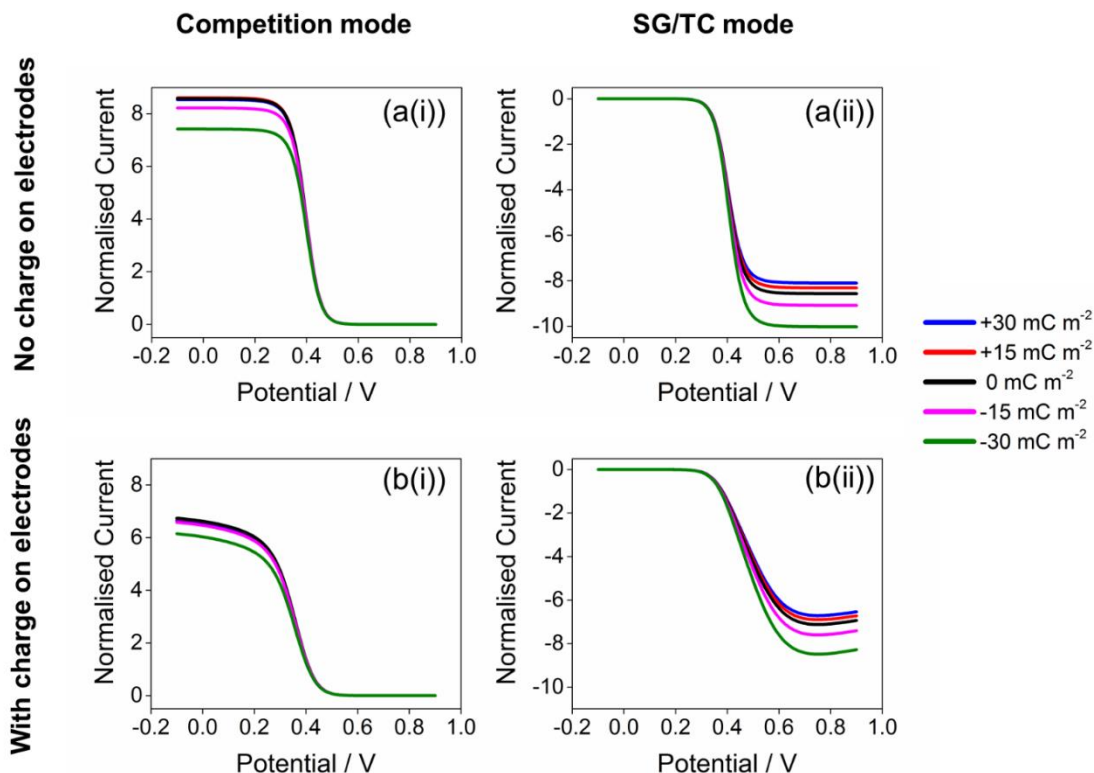


Figure 5. Simulated (i) competition and (ii) SG/TC mode nanogap substrate-voltammetry SECM tip-current vs substrate-potential curves for the oxidation process defined by eq 10 at the substrate electrode, showing the effects of charge on the glass surface that surrounds the UME tip on the voltammogram shape (a) without and (b) with surface charge effects on both electrodes. Simulation parameters were  $L = 0.1$  and  $k_{\text{sub}}^0 = 10 \text{ cm s}^{-1}$ . Other simulation parameters are defined in the text.

In the competition mode, the UME tip is held at a potential ( $E_{\text{UME}} = 0.9 \text{ V}$ ) to oxidise  $\text{M}^+$  to  $\text{M}^{2+}$  at a mass-transport limited rate, while the substrate potential is cycled linearly with respect to time through the range of potentials corresponding to the oxidation of  $\text{M}^+$  to  $\text{M}^{2+}$ . The tip current is determined by the flux of the  $\text{M}^+$  species at the UME tip surface which is in competition with that towards the substrate. It is clear from Figure 5a(i) (no charge on electrode) and 5b(i) (full model with charge on electrode) that in this mode, when the glass surrounding the UME tip is

positively charged, the tip limiting current is enhanced compared to the charge-free glass counterpart. This is because  $M^+$  close to the tip-glass boundary experiences a repulsion from the glass resulting in an enhancement of the flux of  $M^+$  to the active part of the UME tip, as shown in the concentration profile plot in Figure 6a(i), which should be compared to the charge-free case in Figure 6a(ii). Conversely, when the glass is negatively charged, the limiting current is lower than the charge-free counterpart. As seen in Figure 6a(iii), the negatively charged glass surface results in an accumulation of positively charged ions near the glass surface, restricting the redox cycling of  $M^+$  between the tip and substrate.

In the SG/TC mode, the UME tip amperometrically detects substrate-generated  $M^{2+}$  (by reduction to  $M^+$ ) at a fixed tip potential ( $E_{UME} = -0.1$  V) corresponding to transport-limited detection, while the substrate potential is cycled to oxidise  $M^+$  to  $M^{2+}$ . The limiting current in the SG/TC mode is determined by the flux of  $M^{2+}$  species towards the UME tip surface. When the charge on the glass surrounding the UME tip is positively charged, the simulated tip limiting current is diminished compared to the charge-free glass counterpart (Figure 5a(ii) and 5b(ii)). As shown in the concentration profile plot in Figure 6b(i),  $M^{2+}$  species in the gap is repelled from the glass surface, thus diminishing the flux of  $M^{2+}$  towards the UME tip close to the tip/glass boundary, compared to the uncharged glass case in Figure 6b(ii). Conversely, when the glass surface is negatively charged (Figure 6b(iii)), substrate-generated  $M^{2+}$  accumulates near the glass surface resulting in a higher local concentration of  $M^{2+}$  at the tip/glass boundary, which promotes redox

shuttling between the two electrodes and hence resulting in the enhanced limiting current compared to the uncharged glass case.

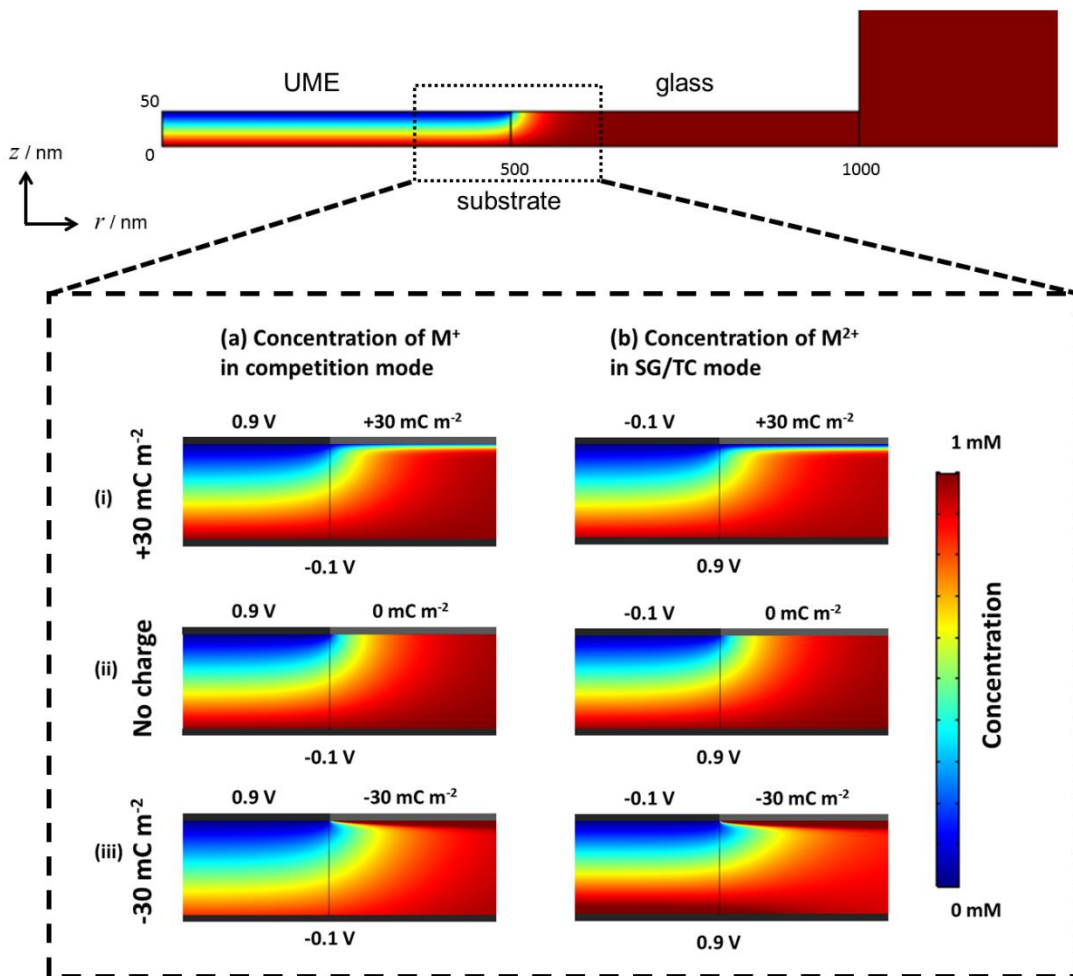


Figure 6. Concentration profiles for (a)  $M^+$  species at the beginning of the competition mode voltammetric scan ( $E_{\text{UME}} = 0.9 \text{ V}$  and  $E_{\text{sub}} = -0.1 \text{ V}$ ) and (b)  $M^{2+}$  at the end of the SG/TC mode voltammetric scan ( $E_{\text{UME}} = -0.1 \text{ V}$  and  $E_{\text{sub}} = 0.9 \text{ V}$ ) for (i)  $+30 \text{ mC m}^{-2}$ , (ii)  $0 \text{ mC m}^{-2}$  and (iii)  $-30 \text{ mC m}^{-2}$  applied to the glass surface surrounding the UME tip. Other simulation parameters are identical to those used for Figure 5a. The top profile is for illustrative purposes only, to show most of the domain from which the zoom profiles are taken, and the vertical line in the profiles marks the edge of the UME tip.



To summarise: surface charge on the glass that encapsulates the UME tip has a strong effect on the limiting current values measured during a voltammetric scan in both the competition and SG/TC modes. An important consequence is that the ‘apparent’ tip-substrate distances resulting from analysis of the simulated curves with a diffusion-only model, as is done, for example, to obtain tip-substrate distances in nanogap SECM [23,36,69], will give the incorrect tip-substrate distances for the paired voltammograms. Interestingly, when a negative charge ( $-30 \text{ mC cm}^{-2}$ ) is considered on the glass surface (as would be typical for aqueous solutions at neutral to basic pH) [44], the apparent tip-substrate distance for the competition mode would be larger than its SG/TC mode counterpart. This phenomenological trend has previously been reported experimentally [36] but was attributed to other effects. Additionally, a further complication is that redox couples could also physically adsorb onto glass and change the charge properties during a voltammetric measurement. For example, our previous measurement of  $\text{FcTMA}^{2+}$  adsorption at glass [30] showed the accumulation of  $\text{FcTMA}^{2+}$  for the glass/solution interface. Adsorption of redox couples, on both the glass and electrodes, even at low levels, will change the interfacial charge and properties dynamically during a voltammetric scan and is increasingly recognised as an important consideration in nanoconfined systems [40,70,71] and we have recently pointed out the importance of thoroughly characterising all surface and interfaces deployed in nanoscale systems [72]. We haven’t treated this aspect herein, in order to keep the modelling tractable, but the model could be developed further in the future.

#### 4.3.2. Effect of charge on the UME and substrate electrodes on paired nanogap voltammograms

We now consider in more detail the effect of charge on both the UME and substrate electrode surfaces. A comparison between the competition and SG/TC modes is shown in Figure 7a(i) and (ii), respectively, where tip-current vs substrate-potential curves, with and without surface charge effects on both the substrate and UME tip electrodes, are considered for an oxidation process at a 0.5  $\mu\text{m}$ -radius UME at  $L = 0.1$ . These simulations also include a surface charge density of  $-30 \text{ mC m}^{-2}$  on the glass surface that encapsulates the UME tip, a typical value for borosilicate in low electrolyte concentration aqueous media ( $\epsilon = 78$ ) [44]. Simulated current-voltage curves, which include the effect of surface charge on the electrode and Frumkin corrected potentials, are significantly different to the counterpart computed without EDL effects. In general, for a given potential, the current is smaller and the voltammogram apparently is less reversible (as defined by reference to a diffusion-only regime) for both the competition and SG/TC modes.

As mentioned above, in both the SG/TC and competition modes, the tip current is dependent on the cycling of a positively charged redox couple between the charged tip and surface. This effect greatly modifies the  $\text{M}^+/\text{M}^{2+}$  distribution and mass transport in the gap, with a significant impact on the voltammetric wave shape (Figure 7(a)(i) and (ii)). This is clearly evident in the concentration profiles of  $\text{M}^+$  and  $\text{M}^{2+}$  shown in Figure 7b(i) across the centre axis of the gap

at  $E_{\text{sub}} = -0.1$  V and  $E_{\text{UME}} = 0.9$  V for the competition mode (i) and  $E_{\text{UME}} = -0.1$  V and  $E_{\text{sub}} = 0.9$  V for the SG/TC mode (ii).

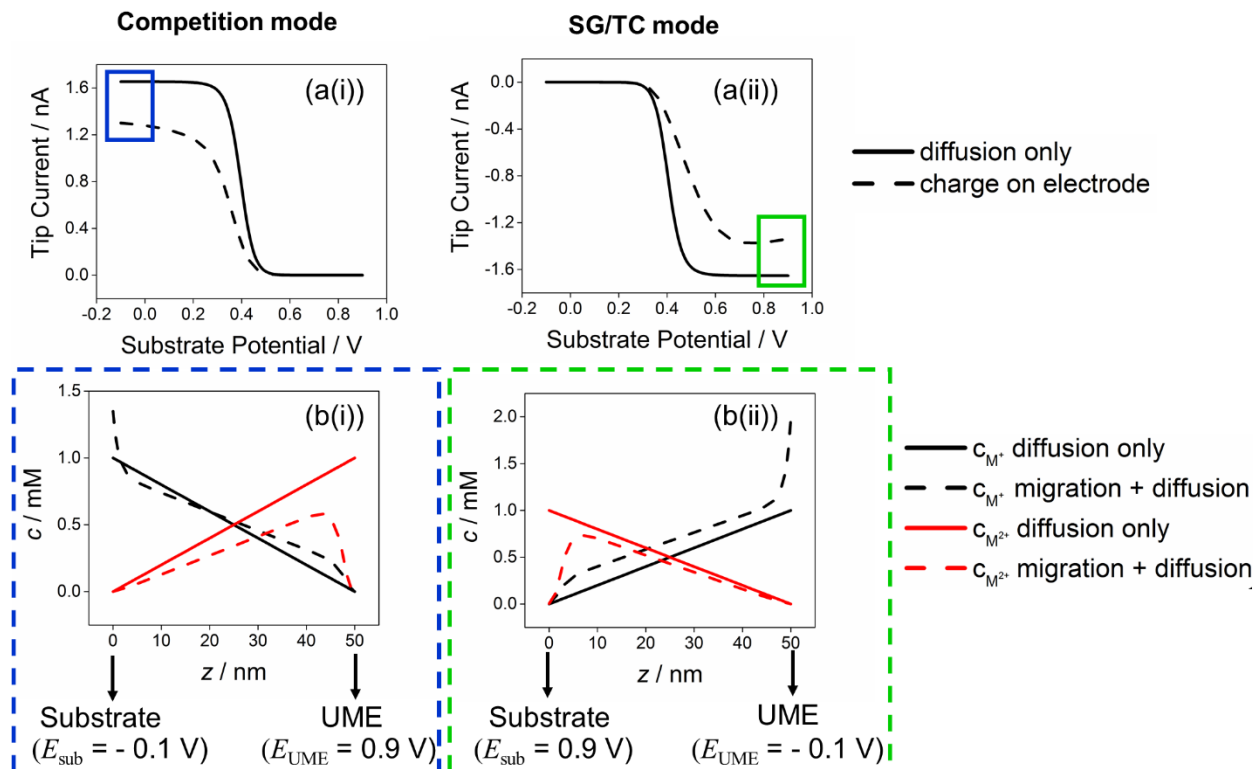


Figure 7. Simulated (a) nanogap substrate-voltammetry SECM tip-current vs substrate-potential curves for the (i) competition and (ii) SG/TC mode for a one-electron oxidation process. The surface charge density at the glass surface that encapsulates the UME was  $-30 \text{ mC m}^{-2}$ . (b) Concentration profiles of  $M^+$  and  $M^{2+}$  in the nanogap along the centre axis of the UME tip ( $z = 0$  and  $50 \text{ nm}$  represent the substrate and tip surface respectively). In the competition mode,  $E_{\text{sub}} = -0.1$  V and  $E_{\text{UME}} = 0.9$  V, while in the SG/TC mode,  $E_{\text{sub}} = 0.9$  V and  $E_{\text{UME}} = -0.1$  V. The solid and dotted lines represent simulated results without and with surface charge effects applied to the both UME and substrate electrode surfaces. Simulation parameters:  $k_{\text{sub}}^0 = 10 \text{ cm s}^{-1}$  and  $L = 0.1$ . Other simulation parameters can be found in the text.

Figure 8a shows voltammograms for both the competition mode and SG/TC mode, when the substrate kinetic values are changed systematically ( $k_{\text{sub}}^0 = 100, 10, 1$  and  $0.5 \text{ cm s}^{-1}$ ) at a fixed

distance,  $L = 0.1$  for the full charge model including the EDL effect on the electrodes, Frumkin corrected potentials, as well as a surface charge density of  $-30 \text{ mC m}^{-2}$  on the glass surface that encapsulates the UME tip. For all  $k_{\text{sub}}^0$  values considered, the currents are smaller than their EDL-free counterpart and, based on the difference in the quartile potentials, appear to have apparently slower kinetics than actually applied in the model (if viewed within the framework of a conventional charge-free diffusion-only model). For some redox systems, it can also be seen that both the competition and SG/TC modes give different limiting currents which, within the confines of a traditional (and typical) [23,36,37] diffusional SECM model, would be interpreted as different apparent tip-substrate distances.

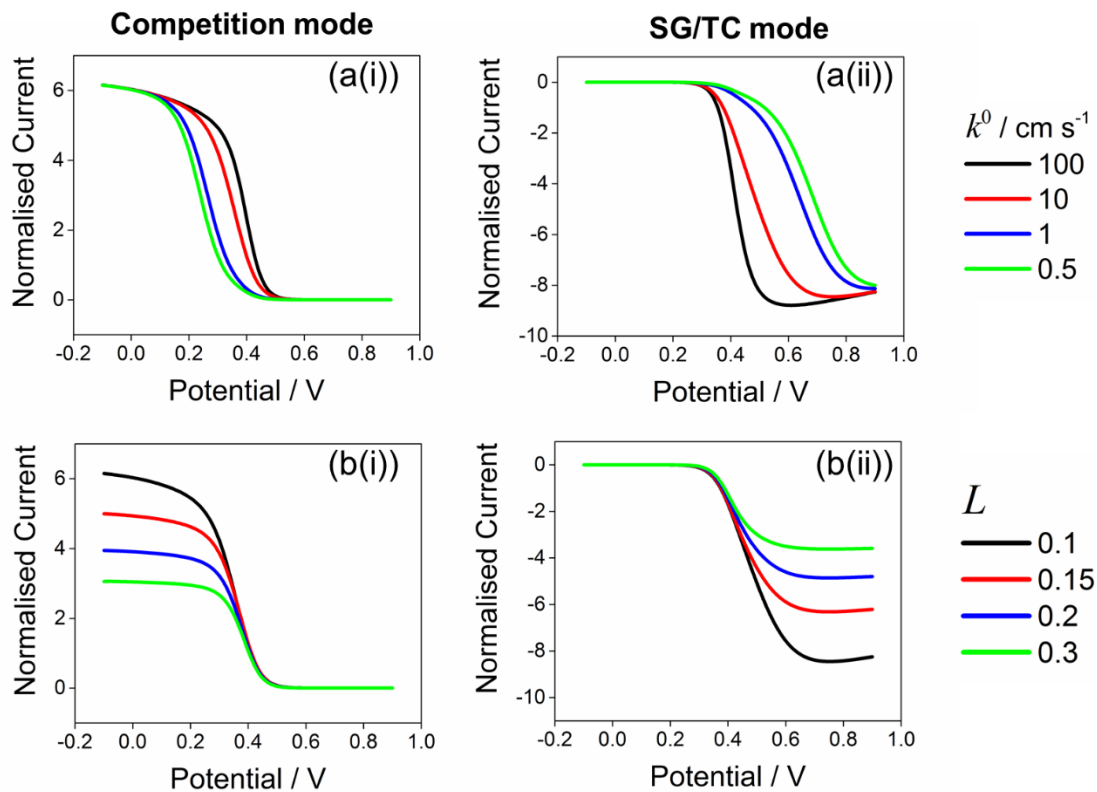


Figure 8. Simulated nanogap substrate-voltammetry SECM tip-current vs substrate potential curves for the oxidation process defined in eq 10 including surface charge and Frumkin corrected potentials on both the tip and substrate electrode surfaces, and a fixed surface charge density of  $-30 \text{ mC m}^{-2}$  on the glass that encapsulates the UME tip. Data are shown for the (i) competition and (ii) SG/TC modes showing the effects of (a) substrate ET kinetics ( $k_{\text{sub}}^0 = 100 \text{ cm s}^{-1}$  (black),  $10 \text{ cm s}^{-1}$  (red),  $1 \text{ cm s}^{-1}$  (blue) and  $0.5 \text{ cm s}^{-1}$  (magenta)) at  $L = 0.1$  and (ii) normalised tip-substrate separation ( $L = 0.1$  (black),  $0.15$  (red),  $0.2$  (blue) and  $0.3$  (magenta)) with  $k_{\text{sub}}^0 = 10 \text{ cm s}^{-1}$ . In the competition mode,  $E_{\text{UME}} = 0.9 \text{ V}$  while in the SG/TC mode,  $E_{\text{UME}} = -0.1 \text{ V}$ . The substrate potential was scanned from  $-0.1 \text{ V}$  to  $0.9 \text{ V}$  at a scan speed of  $50 \text{ mV s}^{-1}$ . Other simulation parameters can be found in the text.

Figure 8b shows simulated UME tip responses when the tip-substrate separation,  $L$ , was varied ( $0.1, 0.15, 0.2$  and  $0.3$ ) with a fixed  $k_{\text{sub}}^0 = 10 \text{ cm s}^{-1}$ . For all tip-substrate distances, the apparent kinetics of the simulated voltammograms are significantly smaller than the known input value ( $k_{\text{sub}}^0 = 10 \text{ cm s}^{-1}$ ) of the simulation if they were analysed using diffusion only assumptions. Further, in all cases, for the competition and SG/TC mode voltammograms have different limiting currents, which would be interpreted as different distances within a simple diffusion-only model [23,24]. It is also important to note that at smaller tip-substrate distances, where the effects of the EDL are most significant, the voltammograms in both the competition and SG/TC mode fail to reach true steady limiting-current values at the most driving potentials. Rather, the voltammograms show an increasing current with applied potential, due to the changing charge on the electrode inducing an increasing migration effect. Anomalous voltammogram shapes can be found in a number of SECM papers [24,36,37,66,70] and have not been commented on or fully explained.

This type of phenomenon could well have some origin in the surface charge effects highlighted herein.

#### 4.3.3. Comparison of simulations of surface charge on both electrodes and glass surfaces

Finally, we consider simulated nanogap substrate-voltammetry SECM results in Figure 9 that compare the following situations: diffusion only (black), the effect of surface charge on the glass ( $-30 \text{ mC m}^{-2}$  in aqueous solution ( $\epsilon = 78$ )) that encapsulates the UME tip, but with no charge on the UME and substrate electrodes (red), the effect of surface charge on the electrode, but with no charge on the glass surface (blue), and the full simulation which includes surface charge and Frumkin corrected potentials on both electrodes and surface charge on the glass surface (green). A value of  $k_{\text{sub}}^0 = 10 \text{ cm s}^{-1}$  was considered, with other parameters defined in the text. It is clear that EDL effects on the electrode surfaces strongly affect the voltammogram shape (the difference in the quartile potentials) and magnitude of current and hence the apparent kinetics, while the surface charge on the glass strongly affects the limiting current magnitudes in both competition and SG/TC modes. Given that these voltammograms are all for the same tip-substrate distance, it is very clear that double layer effects have a profound influence on the voltammetric waveshape.

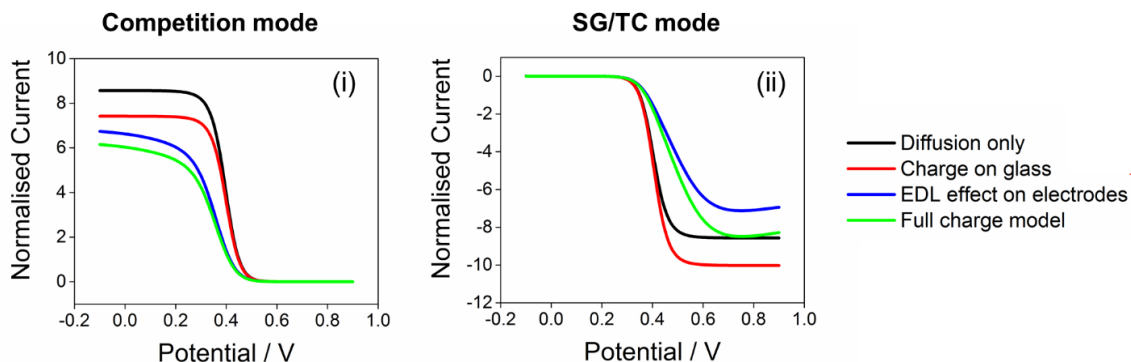


Figure 9. Simulated nanogap substrate-voltammetry SECM tip-current vs substrate-potential curves for an oxidation process comparing plots for diffusion only (black), the effect of charge ( $-30 \text{ mC m}^{-2}$  from ref [44]) on the borosilicate glass encapsulating the UME disk (red), the effect of surface charge and Frumkin corrected potentials on the UME and substrate electrode (blue), and the full charge model including EDL effects at both UME and substrate electrodes and glass surface charge (green). Simulation parameters:  $k_{\text{sub}}^0 = 10 \text{ cm s}^{-1}$ ,  $\rho_G = -30 \text{ mC m}^{-2}$ ,  $L = 0.1$  and  $\nu = 50 \text{ mV s}^{-1}$ . Other simulation parameters can be found in the text.

## 5. Conclusion

In conclusion, we have reported a model for SECM that includes the influence of electrode surface charge, which changes during a voltammetric measurement, and a fixed surface charge on the glass or quartz part of the SECM tip. A typical process involving a redox mediator with a single positive charge that undergoes either a one-electron reduction or one-electron oxidation has been considered, although the model could easily be extended to other cases. Using parameters that are typical for SECM voltammetric measurements in acetonitrile and aqueous solutions, such as 100 mM and 50 mM supporting electrolyte, respectively, a reasonable PZC value and charge magnitudes that are appropriate for the glass or quartz part of the SECM tip, we have shown that

surface charge has a profound influence on voltammetric waveshapes for common SECM modes, namely the tip-voltammetry (feedback mode), and substrate-voltammetry (substrate-generation/tip-collection and competition modes) configurations.

Double layer effects are most significant for the so-called “nanogap” configuration where the SECM tip and substrate electrodes are positioned such that they are within a few 10’s nm of each other, but the effects can also be observed at separations of 100’s nm, as evidenced by simulations and experimental measurements with the  $\text{TTF}/\text{TTF}^{\bullet+}$  and  $\text{TTF}^{\bullet+}/\text{TTF}^{2+}$  redox couples. Surface charge distorts SECM voltammograms, such that they may show non-limiting currents, as evident in a number of examples in the prior literature. Moreover, this distortion leads to voltammetric wave-shapes with kinetics that would appear much slower than the actual electron transfer kinetics operating, if analysed with classical diffusion models and ignoring double layer effects. Furthermore, surface charge results in asymmetric limiting currents of paired SG/TC and competition mode voltammograms and also unequal current magnitudes for the one-electron oxidation and reduction of a singly charged redox species in the tip shielding mode. This would be interpreted as an incorrect tip-substrate distance within the confines of a diffusion-only model.

It is important to emphasise that this work has considered simple models for the charge distribution at the electrode/electrolyte and glass/electrolyte interfaces, and has ignored adsorption of the redox couple, which may be particularly important nanogap geometries. More detailed



models could be implemented, although would require the use of more fitting parameters, and the use of such models would change some the results presented herein. Nonetheless, the basic message conveyed in this paper on the impact of surface charge on SECM is not predicated on particular models for the EDL or the choice of parameter values. Surface charge is an important consideration in SECM measurements with small gaps between the tip and substrate, even with relatively high supporting electrolyte concentrations. Consequently, the physicochemical properties of charged interfaces need to be understood in great detail to properly implement SECM and analyse voltammetric data in this configuration. With this information, and the use of more comprehensive models, and a range of tip-substrate separations, and electrolyte and redox couple concentrations, SECM could be a powerful to elucidate electron transfer kinetics (at larger tip substrate separations and/or higher electrolyte concentrations) and double layer effects (smaller, variable tip substrate separations).

## List of Symbols

$D_i$	Diffusion coefficient of species $i$
$c_i$	Concentration of species $i$
$z_i$	Charge number of species $i$
$J_i$	Flux of species $i$
$k_j^0$	Standard rate constant of reaction $j$
$\alpha_j$	Transfer coefficient of reaction $j$
$E_j^{0'}$	Formal potential of reaction $j$
$\varepsilon$	Dielectric constant of solution of interest

$\epsilon_{\text{HL}}$	Dielectric constant within the Helmholtz layer
$d_{\text{HL}}$	Dimension of the Helmholtz layer
$\rho$	Surface charge density
$F$	Faraday constant
$R$	Gas constant
$T$	Absolute temperature
$\phi$	Electric potential
$E_{\text{sub}}$	Potential applied to the substrate electrode
$E_{\text{UME}}$	Potential applied to the UME electrode
$E_{\text{PZC}}$	Potential of zero charge
$\nu$	Potential sweep rate
$i_{\text{lim,red}}$	Reduction limiting current
$i_{\text{lim,ox}}$	Oxidation limiting current

## Acknowledgements

We thank the University of Warwick for support for ST and the Leverhulme Trust for support for DP. PRU gratefully acknowledges a Royal Society Wolfson Research Merit Award.

## Dedication

PRU dedicates this paper to the memory of Professor Roger Parsons. As a graduate student in the 1980s, PRU was inspired by many seminal papers in *J. Electroanal. Chem.*, then under the

Editorship of Roger, and received encouragement from Roger at the start of his independent career at Warwick, which was greatly appreciated.

## References

- [1] R. Parsons, The electrical double layer: recent experimental and theoretical developments, *Chem. Rev.* 90 (1990) 813–826. doi:10.1021/cr00103a008.
- [2] H. Helmholtz, Studien über electrische Grenzsichten, *Ann. Der Phys. Und Chemie.* 243 (1879) 337–382. doi:10.1002/andp.18792430702.
- [3] J. Davis, R. James, J. Leckie, Surface Ionization and Complexation at the Oxide / Water Interface, *J. Colloid Interface Sci.* 63 (1978) 480–499. doi:10.1016/S0021-9797(78)80009-5.
- [4] K.B. Oldham, A Gouy-Chapman-Stern model of the double layer at a (metal)/(ionic liquid) interface, *J. Electroanal. Chem.* 613 (2008) 131–138. doi:10.1016/j.jelechem.2007.10.017.
- [5] S. McLaughlin, The Electrostatic Properties Of Membranes, *Annu. Rev. Biophys. Biomol. Struct.* 18 (1989) 113–136. doi:10.1146/annurev.biophys.18.1.113.
- [6] W. Stumm, J.J. Morgan, *Aquatic Chemistry: Chemical Equilibria and Rates in Natural Waters*, 3rd ed., Wiley, 1995.
- [7] Y. Gao, Y. Liu, S. Chen, A Theoretical Consideration of Ion Size Effects on the Electric Double Layer and Voltammetry of Nanometer-sized Disk Electrodes, *Faraday Discuss.* (2016) 1–13. doi:10.1039/C6FD00087H.
- [8] C.P. Smith, H.S. White, Theory of the voltammetric response of electrodes of submicron dimensions. Violation of electroneutrality in the presence of excess supporting electrolyte, *Anal. Chem.* 65 (1993) 3343–3353. doi:10.1021/ac00071a002.
- [9] R. He, S. Chen, F. Yang, B. Wu, Dynamic diffuse double-layer model for the electrochemistry of nanometer-sized electrodes, *J. Phys. Chem. B.* 110 (2006) 3262–3270. doi:10.1021/jp060084j.
- [10] J.D. Norton, H.S. White, S.W. Feldberg, Effect of the Electrical Double Layer on Voltammetry at Microelectrodes, *J. Phys. Chem.* 94 (1990) 6772–6780. doi:10.1021/j100380a044.
- [11] P. Sun, M. V. Mirkin, Electrochemistry of individual molecules in zeptoliter volumes, *J. Am. Chem. Soc.* 130 (2008) 8241–8250. doi:10.1021/ja711088j.
- [12] S. Yu, L. Yuwen, L. Zhixiu, X. Lu, W. Aili, C. Shengli, On the applicability of conventional

- voltammetric theory to nanoscale electrochemical interfaces, *J. Phys. Chem. C.* 113 (2009) 9878–9883. doi:10.1021/jp902311h.
- [13] Y. Liu, R. He, Q. Zhang, S. Chen, Theory of electrochemistry for nanometer-sized disk electrodes, *J. Phys. Chem. C.* 114 (2010) 10812–10822. doi:10.1021/jp9102806.
  - [14] J.J. Watkins, H.S. White, The Role of the Electrical Double Layer and Ion Pairing on the Electrochemical Oxidation of Hexachloroiridate ( III ) at Pt Electrodes of Nanometer Dimensions, (2004) 5474–5483. doi: 10.1021/la0496993
  - [15] J. Xiong, Q. Chen, M.A. Edwards, H.S. White, Ion Transport within High Electric Fields in Nanogap Electrochemical Cells, *ACS Nano.* 9 (2015) 8520–8529. doi:10.1021/acsnano.5b03522.
  - [16] Q. Chen, K. McKelvey, M.A. Edwards, H.S. White, Redox Cycling in Nanogap Electrochemical Cells. The Role of Electrostatics in Determining the Cell Response, *J. Phys. Chem. C.* 120 (2016) 17251–17260. doi:10.1021/acs.jpcc.6b05483.
  - [17] J.H. Bae, Y. Yu, M. V. Mirkin, Diffuse Layer Effect on Electron-Transfer Kinetics Measured by Scanning Electrochemical Microscopy (SECM), *J. Phys. Chem. Lett.* 8 (2017) 1338–1342. doi:10.1021/acs.jpcclett.7b00161.
  - [18] L. Fan, Y. Liu, J. Xiong, H.S. White, S. Chen, Electron-Transfer Kinetics and Electric Double Layer Effects in Nanometer-Wide Thin-Layer Cells, *ACS Nano.* 8 (2014) 10426–10436. doi:10.1021/nn503780b.
  - [19] S. Chen, Y. Liu, Electrochemistry at nanometer-sized electrodes, *Phys. Chem. Chem. Phys.* 16 (2014) 635–652. doi:10.1039/C3CP53773K.
  - [20] S. Chen, Y. Liu, J. Chen, Heterogeneous electron transfer at nanoscopic electrodes: importance of electronic structures and electric double layers, *Chem. Soc. Rev.* 43 (2014) 5372. doi:10.1039/C4CS00087K.
  - [21] P. Sun, M. V. Mirkin, Kinetics of Electron-Transfer Reactions at Nanoelectrodes, *Anal. Chem.* 78 (2006) 6526–6534. doi:10.1021/ac060924q.
  - [22] J. Velmurugan, P. Sun, M. V. Mirkin, Scanning Electrochemical Microscopy with Gold Nanotips: The Effect of Electrode Material on Electron Transfer Rates, *J. Phys. Chem. C.* 113 (2009) 459–464. doi:10.1021/jp808632w.
  - [23] N. Nioradze, J. Kim, S. Amemiya, Quasi-Steady-State Voltammetry of Rapid Electron Transfer Reactions at the Macroscopic Substrate of the Scanning Electrochemical Microscope, *Anal. Chem.* 83 (2011) 828–835. doi:10.1021/ac102352v.
  - [24] M. Shen, A.J. Bard, Localized electron transfer and the effect of tunneling on the rates of Ru(bpy)<sub>3</sub>(2+) oxidation and reduction as measured by scanning electrochemical microscopy., *J. Am. Chem. Soc.* 133 (2011) 15737–42. doi:10.1021/ja206136h.
  - [25] C.B. Ekanayake, M.B. Wijesinghe, C.G. Zoski, Determination of Heterogeneous Electron Transfer and Homogeneous Comproportionation Rate Constants of Tetracyanoquinodimethane Using Scanning Electrochemical Microscopy, *Anal. Chem.* 85 (2013) 4022–4029. doi:10.1021/ac400256x.

- [26] C.B. Ekanayake, C.G. Zoski, Scanning Electrochemical Microscopy Determination of Heterogeneous Electron Transfer and Homogeneous Association and Comproportionation Rate Constants of Anthrarufin, *Electroanalysis*. 28 (2016) 2424–2434. doi:10.1002/elan.201600259.
- [27] A. Oleinick, Y. Yu, I. Svir, M. V. Mirkin, C. Amatore, Theory and Simulations for the Electron-Transfer/Ion-Transfer Mode of Scanning Electrochemical Microscopy in the Presence or Absence of Homogenous Kinetics, *ChemElectroChem*. 4 (2017) 287–295. doi:10.1002/celec.201600583.
- [28] P.R. Unwin, A.J. Bard, Scanning electrochemical microscopy. 14. Scanning electrochemical microscope induced desorption: a new technique for the measurement of adsorption/desorption kinetics and surface diffusion rates at the solid/liquid interface, *J. Phys. Chem.* 96 (1992) 5035–5045. doi:10.1021/j100191a055.
- [29] J. Rodríguez-López, A.J. Bard, Scanning Electrochemical Microscopy: Surface Interrogation of Adsorbed Hydrogen and the Open Circuit Catalytic Decomposition of Formic Acid at Platinum, *J. Am. Chem. Soc.* 132 (2010) 5121–5129. doi:10.1021/ja9090319.
- [30] S. Tan, J. Zhang, A.M. Bond, J. V. Macpherson, P.R. Unwin, Impact of Adsorption on Scanning Electrochemical Microscopy Voltammetry and Implications for Nanogap Measurements, *Anal. Chem.* 88 (2016) 3272–3280. doi:10.1021/acs.analchem.5b04715.
- [31] J. Zhang, C.J. Slevin, C. Morton, P. Scott, D.J. Walton, P.R. Unwin, Scanning electrochemical microscopy (SECM) feedback approach for measuring lateral proton diffusion in langmuir monolayers: theory and application, *J. Phys. Chem. B.* 105 (2001) 11120–11130. doi:10.1039/b111399b.
- [32] J. Zhang, P.R. Unwin, Proton diffusion at phospholipid assemblies., *J. Am. Chem. Soc.* 124 (2002) 2379–83. doi:10.1021/ja012074w.
- [33] A.P. O’Mullane, J. V. Macpherson, P.R. Unwin, J. Cervera-Montesinos, J.A. Manzanares, F. Frehill, J.G. Vos, Measurement of Lateral Charge Propagation in [ Os ( bpy ) <sub>2</sub> ( PVP )<sub>n</sub> Cl ] Cl Thin Films : A Scanning Electrochemical Microscopy Approach, *J. Phys. Chem. B.* 108 (2004) 7219–7227. doi:10.1021/jp049500v
- [34] A.L. Whitworth, D. Mandler, P.R. Unwin, Theory of scanning electrochemical microscopy (SECM) as a probe of surface conductivity, *Phys. Chem. Chem. Phys.* 7 (2005) 356–365. doi:10.1039/b407397e.
- [35] F. Hauquier, J. Ghilane, B. Fabre, P. Hapiot, Conducting ferrocene monolayers on nonconducting surfaces., *J. Am. Chem. Soc.* 130 (2008) 2748–9. doi:10.1021/ja711147f.
- [36] N. Nioradze, R. Chen, N. Kurapati, A. Khvataeva-Domanov, S. Mabic, S. Amemiya, Organic Contamination of Highly Oriented Pyrolytic Graphite As Studied by Scanning Electrochemical Microscopy, *Anal. Chem.* 87 (2015) 4836–4843. doi:10.1021/acs.analchem.5b00213.
- [37] R. Chen, N. Nioradze, P. Santhosh, Z. Li, S.P. Surwade, G.J. Shenoy, D.G. Parobek, M.A. Kim, H. Liu, S. Amemiya, Ultrafast Electron Transfer Kinetics of Graphene Grown by

- Chemical Vapor Deposition, *Angew. Chemie Int. Ed.* 54 (2015) 15134–15137. doi:10.1002/anie.201507005.
- [38] B. Zhang, Y. Zhang, H.S. White, The nanopore electrode, *Anal. Chem.* 76 (2004) 6229–6238. doi:10.1021/ac049288r.
- [39] K. Mathwig, S.G. Lemay, Mass transport in electrochemical nanogap sensors, *Electrochim. Acta.* 112 (2013) 943–949. doi:10.1016/j.electacta.2013.05.142.
- [40] D. Mampallil, K. Mathwig, S. Kang, S.G. Lemay, Reversible Adsorption of Outer-Sphere Redox Molecules at Pt Electrodes, *J. Phys. Chem. Lett.* 5 (2014) 636–640. doi:10.1021/jz402592n.
- [41] A.J. Bard, F.R.F. Fan, J. Kwak, O. Lev, Scanning electrochemical microscopy. Introduction and principles, *Anal. Chem.* 61 (1989) 132–138. doi: 10.1021/ac00177a011
- [42] D. Momotenko, F. Cortes-Salazar, J. Josserand, S. Liu, Y. Shao, H.H. Girault, Ion current rectification and rectification inversion in conical nanopores : a perm-selective view, *Phys. Chem. Chem. Phys.* 13 (2011) 5430–5440. doi:10.1039/c0cp02595j.
- [43] C. Wei, A.J. Bard, S.W. Feldberg, Current Rectification at Quartz Nanopipet Electrodes, *Anal. Chem.* 69 (1997) 4627–4633. doi:10.1021/ac970551g.
- [44] D. Perry, D. Momotenko, R.A. Lazenby, M. Kang, P.R. Unwin, Characterization of Nanopipettes, *Anal. Chem.* 88 (2016) 5523–5530. doi:10.1021/acs.analchem.6b01095.
- [45] H.S. White, A. Bund, Ion current rectification at nanopores in glass membranes, *Langmuir.* 24 (2008) 2212–2218. doi:10.1021/la702955k.
- [46] A. Page, D. Perry, P. Young, D. Mitchell, B.G. Frenguelli, P.R. Unwin, Fast Nanoscale Surface Charge Mapping with Pulsed-Potential Scanning Ion Conductance Microscopy, *Anal. Chem.* 88 (2016) 10854–10859. doi:10.1021/acs.analchem.6b03744.
- [47] K. McKelvey, S.L. Kinnear, D. Perry, D. Momotenko, P.R. Unwin, Surface Charge Mapping with a Nanopipette, *J. Am. Chem. Soc.* 136 (2014) 13735–13744. doi:10.1021/ja506139u.
- [48] K. McKelvey, D. Perry, J.C. Byers, A.W. Colburn, P.R. Unwin, Bias modulated scanning ion conductance microscopy, *Anal. Chem.* 86 (2014) 3639–3646. doi:10.1021/ac5003118.
- [49] D. Perry, R. Al Botros, D. Momotenko, S.L. Kinnear, P.R. Unwin, Simultaneous Nanoscale Surface Charge and Topographical Mapping, *ACS Nano.* 9 (2015) 7266–7276. doi:10.1021/acsnano.5b02095.
- [50] N. Sa, W.J. Lan, W. Shi, L.A. Baker, Rectification of ion current in nanopipettes by external substrates, *ACS Nano.* 7 (2013) 11272–11282. doi:10.1021/nn4050485.
- [51] M. Bendikov, F. Wudl, D.F. Perepichka, Tetrathiafulvalenes, Oligoacenes, and Their Buckminsterfullerene Derivatives: The Brick and Mortar of Organic Electronics, *Chem. Rev.* 104 (2004) 4891–4946. doi:10.1021/cr030666m.
- [52] C.G. Zoski, C.R. Luman, J.L. Fernández, A.J. Bard, Scanning electrochemical microscopy. 57. SECM tip voltammetry at different substrate potentials under quasi-steady-state and

- steady-state conditions, *Anal. Chem.* 79 (2007) 4957–4966. doi:10.1021/ac070021c.
- [53] R.D. Martin, P.R. Unwin, Scanning electrochemical microscopy: theory and experiment for the positive feedback mode with unequal diffusion coefficients of the redox mediator couple, *J. Electroanal. Chem.* 439 (1997) 123–136. doi:10.1016/S0022-0728(97)00377-X.
  - [54] C.G. Williams, M.A. Edwards, A.L. Colley, J. V Macpherson, P.R. Unwin, Scanning Micropipet Contact Method for High-Resolution Imaging of Electrode Surface Redox Activity, *Anal. Chem.* 81 (2009) 2486–2495. doi:10.1021/ac802114r.
  - [55] C.D. Baer, N.J. Stone, D.A. Sweigart, Fabrication of platinum-disk ultramicroelectrodes, *Anal. Chem.* 60 (1988) 188–191. doi:10.1021/ac00153a021.
  - [56] K. McKelvey, M.A. Edwards, P.R. Unwin, Intermittent Contact–Scanning Electrochemical Microscopy (IC–SECM): A New Approach for Tip Positioning and Simultaneous Imaging of Interfacial Topography and Activity, *Anal. Chem.* 82 (2010) 6334–6337. doi:10.1021/ac101099e.
  - [57] D. Momotenko, H.H. Girault, Scan-rate-dependent ion current rectification and rectification inversion in charged conical nanopores, *J. Am. Chem. Soc.* 133 (2011) 14496–14499. doi:10.1021/ja2048368.
  - [58] A. Page, D. Perry, P.R. Unwin, Multifunctional scanning ion conductance microscopy, *Proc. R. Soc. A Math. Phys. Eng. Sci.* 473 (2017) 20160889. doi:10.1098/rspa.2016.0889.
  - [59] X. Yin, S. Zhang, Y. Dong, S. Liu, J. Gu, Y. Chen, X. Zhang, X. Zhang, Y. Shao, Ionic Current Rectification in Organic Solutions with Quartz Nanopipettes, *Anal. Chem.* 87 (2015) 9070–9077. doi:10.1021/acs.analchem.5b02337.
  - [60] C. Lefrou, A unified new analytical approximation for positive feedback currents with a microdisk SECM tip, *J. Electroanal. Chem.* 592 (2006) 103–112. doi:10.1016/j.jelechem.2006.05.003.
  - [61] P.R. Unwin, A.J. Bard, Scanning electrochemical microscopy. 9. Theory and application of the feedback mode to the measurement of following chemical reaction rates in electrode processes, *J. Phys. Chem.* 95 (1991) 7814–24. doi:10.1021/ja9096187.
  - [62] G.M. Torrie, J.P. Valleau, Electrical double layers. I. Monte Carlo study of a uniformly charged surface, *J. Chem. Phys.* 73 (1980) 5807–5816. doi:10.1063/1.440065.
  - [63] M. V Mirkin, A.J. Bard, Simple analysis of quasi-reversible steady-state voltammograms, *Anal. Chem.* 64 (1992) 2293–2302. doi:10.1021/ac00043a020.
  - [64] J. Varghese, H. Wang, L. Pilon, Simulating electric double layer capacitance of mesoporous electrodes with cylindrical pores, *J. Electrochem. Soc.* 158 (2011) A1106–A1114. doi:10.1149/1.3622342
  - [65] H. V. Patten, S.C.S. Lai, J. V. MacPherson, P.R. Unwin, Active sites for outer-sphere, inner-sphere, and complex multistage electrochemical reactions at polycrystalline boron-doped diamond electrodes (pBDD) revealed with scanning electrochemical cell microscopy (SECCM), *Anal. Chem.* 84 (2012) 5427–5432. doi:10.1021/ac3010555.

- [66] S. Tan, R.A. Lazenby, K. Bano, J. Zhang, A.M. Bond, J. V Macpherson, P.R. Unwin, Comparison of fast electron transfer kinetics at platinum, gold, glassy carbon and diamond electrodes using Fourier-transformed AC voltammetry and scanning electrochemical microscopy, *Phys. Chem. Chem. Phys.* 19 (2017) 8726–8734. doi:10.1039/C7CP00968B.
- [67] A.J. Bard, M. V Mirkin, P.R. Unwin, D. Wipf, Scanning Electrochemical Microscopy. 12. Theory and Experiment of the Feedback Mode with Finite Heterogeneous Electron-Transfer Kinetics and Arbitrary Substrate Size, *J. Phys. Chem.* 96 (1992) 1861–1868. doi:10.1021/j100183a064
- [68] R.D. Martin, P.R. Unwin, Theory and Experiment for the Substrate Generation/Tip Collection Mode of the Scanning Electrochemical Microscope: Application as an Approach for Measuring the Diffusion Coefficient Ratio of a Redox Couple, *Anal. Chem.* 70 (1998) 276–284. doi:10.1021/ac970681p.
- [69] R. Chen, R.J. Balla, Z. Li, H. Liu, S. Amemiya, Origin of Asymmetry of Paired Nanogap Voltammograms Based on Scanning Electrochemical Microscopy: Contamination Not Adsorption, *Anal. Chem.* 88 (2016) 8323–8331. doi:10.1021/acs.analchem.6b02273.
- [70] K. Mathwig, H.R. Zafarani, J.M. Speck, S. Sarkar, H. Lang, S.G. Lemay, L. Rassaei, O.G. Schmidt, Potential-Dependent Stochastic Amperometry of Multiferoxythiophenes in an Electrochemical Nanogap Transducer, *J. Phys. Chem. C.* 120 (2016) 23262–23267. doi:10.1021/acs.jpcc.6b07320
- [71] S. Kang, A.F. Nieuwenhuis, K. Mathwig, D. Mampallil, Z.A. Kostichenko, S.G. Lemay, Single-molecule electrochemistry in nanochannels: probing the time of first passage, *Faraday Discuss.* 193 (2016) 41–50. doi:10.1039/C6FD00075D
- [72] S. Tan, J. Zhang, A.M. Bond, J. V Macpherson, P.R. Unwin, Influence of Tip and Substrate Properties and Nonsteady-State Effects on Nanogap Kinetic Measurements: Response to Comment on “Impact of Adsorption on Scanning Electrochemical Microscopy Voltammetry and Implications for Nanogap Measurements,” *Anal. Chem.* 89 (2017) 7273–7276. doi:10.1021/acs.analchem.7b01664
- [73] I. Dumitrescu, J.P. Edgeworth, P.R. Unwin, J. V. Macpherson, Ultrathin Carbon Nanotube Mat Electrodes for Enhanced Amperometric Detection, *Adv. Mater.* 21 (2009) 3105–3109. doi:10.1002/adma.200900402.